

2010

Finite Element Analysis of a Nose Gear During Landing

Thoai D. Nguyen
University of North Florida

Follow this and additional works at: <https://digitalcommons.unf.edu/etd>



Part of the [Mechanical Engineering Commons](#)

Suggested Citation

Nguyen, Thoai D., "Finite Element Analysis of a Nose Gear During Landing" (2010). *UNF Graduate Theses and Dissertations*. 215.

<https://digitalcommons.unf.edu/etd/215>

This Master's Thesis is brought to you for free and open access by the Student Scholarship at UNF Digital Commons. It has been accepted for inclusion in UNF Graduate Theses and Dissertations by an authorized administrator of UNF Digital Commons. For more information, please contact [Digital Projects](#).

© 2010 All Rights Reserved

FINITE ELEMENT ANALYSIS OF A NOSE GEAR DURING LANDING

by

Thoai D. Nguyen

A thesis submitted to the
School of Engineering
in partial fulfillment of the requirements for the degree of

Master of Science in Mechanical Engineering

UNIVERSITY OF NORTH FLORIDA
COLLEGE OF COMPUTING, ENGINEERING AND CONSTRUCTION

April 2010

The thesis "Finite element analysis of a nose gear during landing" submitted by Thoai Nguyen in partial fulfillment of the requirements for the degree of Master of Science in Mechanical Engineering has been

Approved by the thesis committee:

(Date)

Signature Deleted

3/9/10

Dr. Alexandra Schonning
Thesis Advisor

Signature Deleted

3/9/10

Dr. Paul Eason
Committee member

Signature Deleted

3/9/10

Dr. David Nicholson
Committee member

Accepted for the School of Engineering:
Signature Deleted

3/23/10

Dr. Daniel Cox
Director of School of Engineering

Signature Deleted

3/30/10

Dr. Peter Braza
Dean of College of Computing, Engineering and Construction

Accepted for the University:
Signature Deleted

4-27-10

Dr. Len Roberson
Dean of Graduate School

ACKNOWLEDGEMENTS

I would like to express my deepest appreciation to my advisor, Dr. Alexandra Schonning. Thank you so much for your support and guidance during my graduate studies at the University of North Florida.

I would like to thank my family for their encouragement and support. I also would like to thank Team Jas Aviation for sharing some of the Twin Otter data and experiences. This thesis would not have been possible without the help, support, and guidance from Dr. Schonning, my family, Team Jas, and my co-advisers Dr. Nicholson and Dr. Eason.

TABLE OF CONTENTS

LIST OF FIGURES	v
LIST OF TABLES	vi
ABSTRACT	vii
SYMBOLS AND ABBREVIATIONS	viii
Chapter 1: INTRODUCTION.....	1
Chapter 2: LITERATURE REVIEW.....	4
2.1 BACKGROUND.....	4
2.2 EYE-BAR THEORY	5
2.3 TIRE/WHEEL INTERFACE.....	6
2.4 SHOCK ABSORBER.....	8
2.5 MATERIALS.....	10
2.6 FINITE ELEMENT METHOD (FEM)	11
Chapter 3: MODELING AND LOADING ANALYSIS.....	13
3.0 MODELING OVERVIEW	13
3.1 COMPUTER AIDED DESIGN	13
3.2 FORCE DETERMINATION	14
3.2.1 Ground forces.....	14
3.2 SHOCK ABSORBER FORCES	18
Chapter 4: FINITE ELEMENT ANALYSIS.....	22
4.0 BOUNDARY CONDITIONS	22
4.1 CONTACTS	24
4.2 LOADING.....	25
4.3 MESHING	28
4.4 MATERIAL SELECTION	32
Chapter 5: RESULTS	34
Chapter 6: DISCUSSION AND CONCLUSIONS	40
REFERENCES.....	41
APPENDIX A.....	44
BASIC LANDING CONDITIONS	44

LIST OF FIGURES

FIGURE 1: TWIN OTTER AIRCRAFT SHOWING THE LOCATIONS OF LANDING GEARS	3
FIGURE 2: BREAKDOWN OF THE NOSE GEAR.....	3
FIGURE 3: EYE-BAR LOADING	5
FIGURE 4: NOSE GEAR PARTS FOR FEM	13
FIGURE 5: LANDING CONFIGURATION	15
FIGURE 6: DIMENSIONAL SCHEMATIC.....	15
FIGURE 7: CROSS SECTION OF TIRE/WHEEL	17
FIGURE 8: CONTACT PATCH REGION	17
FIGURE 9: SHOCK ABSORBER CROSS SECTION	19
FIGURE 10: FRICTIONAL FORCE FROM SEALS	21
FIGURE 11: FIXED BOUNDARY CONDITION AT HIGHLIGHTED SURFACES.....	22
FIGURE 12: BOUNDARY CONDITION	23
FIGURE 13: CONTACTS OPTIONS	24
FIGURE 14: INFLATION PRESSURE DISTRIBUTION AROUND THE WHEEL	26
FIGURE 15: BEAD SEAT PRESSURE CAUSED BY VERTICAL FORCE	26
FIGURE 16: DRAG FORCE AT THE POINT OF CONTACT WITH GROUND	27
FIGURE 17: SHOCK ABSORBER FORCE AT PISTON	28
FIGURE 18: DIFFERENT TYPES OF BRICK ELEMENT	30
FIGURE 19: NOSE GEAR MESH.....	31
FIGURE 20: SURFACE MATCHING	31
FIGURE 21: SURFACE NOT MATCHING	32
FIGURE 22: WHEEL ASSEMBLY - STRESS CONCENTRATION	34
FIGURE 23: STRESS AND DISPLACEMENT	35
FIGURE 24: STRESS AND DISPLACEMENT OF THE CYLINDER	36
FIGURE 25: STRESS AND DISPLACEMENT OF THE FORK	37
FIGURE 26: STRESS AND DISPLACEMENT OF THE WHEEL ASSEMBLY	38
FIGURE 27: STRESS RESULTS OF THE PISTON TUBE, LOCKNUT AND AXLE	38

LIST OF TABLES

TABLE 1: BOUNDARY CONDITIONS	23
TABLE 2: USES OF EACH CONTACT IN LINEAR STATIC STRESS	24
TABLE 3: CONTACT SURFACES	25
TABLE 4: ELEMENT DESCRIPTIONS	29
TABLE 5: ELEMENT TYPES AND QUANTITIES	30
TABLE 6: MATERIAL IDENTIFICATION.....	33
TABLE 7: MATERIAL PROPERTIES	33
TABLE 8: STRESS AND DISPLACEMENT RESULTS.....	35
TABLE 9: FACTORS OF SAFETY	37

ABSTRACT

Nose gear failure is a high concern in the aviation industries. According to the Federal Aviation Administration reports, 55% of aircraft failures occur during takeoff and landing while 45% of failures occur during flight. The objective of this thesis is to determine the stress behavior and the displacement of a nose gear of an aircraft during landing using structural finite element analysis. The nose gear was first modeled using computer-aided design software and then imported into finite element software. The external forces were determined analytically and the interactions between components were carefully modeled using contact analysis. The tire was modeled using the eye-bar theory. The results obtained in this work are consistent with the Federal Aviation Administration's recommendations for physical testing.

SYMBOLS AND ABBREVIATIONS

A_o	: Orifice area
A_p	: Piston area
a	: Tire radius of the wheel
b	: Bead seat of the wheel
b'	: Distance from the center of gravity of the airplane to the main wheel
d'	: Distance from the nose wheel to the main wheel
cg	: Center of Gravity
C_d	: Discharge coefficient
d_o	: Orifice diameter
d_p	: Piston diameter
E	: Young modulus
F_a	: Pneumatic force
F_f	: Friction force
F_h	: Hydraulic force
L	: Wing lift to weight ratio
M	: Bending moment
N_1	: Normal force at location 1
N_2	: Normal force at location 2
n	: Limit inertia load factor
g	: Gas constant
p_o	: Inflation pressure
p_a	: Air pressure
V_f	: Reaction force at the nose wheel
W	: Gross weight of the aircraft
y_s	: Piston stroke height
\dot{y}_s	: Piston stroke velocity
ρ_o	: Oil density
ρ_a	: Air density
σ_u	: Ultimate tensile strength
σ_v	: Von mises stress
σ_y	: Yield stress
FAA	: Federal Aviation Administration

Chapter 1: INTRODUCTION

Prior to 1942, the National Advisory Committee for Aeronautics (NACA) spent several years studying the characteristics of the landing gears during landing. Many aircrafts ranging from 1000 lbs. to 50,000 lbs. were used in the study. Until September 1942, the NACA technical note 863 came out to report the results and formulas for all external forces on the nose, main and rear landing gear [1]. Until August 1, 1950, Aeronautical Standard AS227C was used as the guidance to test all the wheels and brakes before installation onto the aircrafts.

Approximately a decade after the introduction of AS227C, Technical Standard Order (TSO) C26a was implemented on June 1, 1961. Today TSO C26 is at revision D. There are two required TSO's in the nose landing gear: TSO C26 for the wheel and brakes and TSO C62 for the tire. Any other components in the nose gear besides the wheel, brakes and tire do not require any physical testing specifications. Many manufacturers do not use FEM to test the nose landing gear because the FAA does not require FEM as part of the approval process. This thesis will help landing gear manufacturers answer many questions related to the nose gear during landing, and these answers can be used in the early stage of future the designs.

For example, this analysis will help manufacturers determine what part in the nose gear will yield the highest stresses and at what location. It will help determine how to design, analyze and optimize the nose gear properly so physical testing can be used for verification instead of trial and error. The cost for physical testing of the wheel assembly is as approximately \$85,000 and can take up to 6 months; therefore, optimizing the design to its best performance before physical testing is very important. The main focus

of the analysis in this thesis is the moment during landing; however, the model is set to be used for other load case scenarios.

Since the birth of Aviation, aircraft landing gears have been essential components of every aircraft. They are used during takeoff, landing and ground operation to support the aircraft. One hundred and ten records have been found related to landing gears in the Service Difficulty Report in the United States in 2009 [2]. All reports have been recorded due to some level of difficulties to the landing gears. The difficulties vary from a nose gear to a main gear to a tail gear.

Aircrafts have several landing gear configurations, such as tricycle gear with nose wheel and two main wheels, or conventional gear with one tail and two main wheels. Different configurations will result in the different load paths and stress behaviors. This thesis focuses on the nose gear of the Twin Otter. Twin Otter aircraft was originally manufactured by DeHavilland Canada and today is owned by Viking Air.

Although the finite element analysis (FEA) theory was first introduced in 1943 by Richard Courant, the study of the nose gear using FEA is not heavily studied and published. Most of the studies have been performed by physical testing by landing gear manufacturers. In order to perform FEA, many steps have to be completed in order to obtain accurate results, including the application of the parts, and the appropriate assumptions. All components making up the nose gear must be modeled in three-dimensional (3-D) computer-aided design (CAD) software. In this study, the SolidWorks CAD software was used. Once 3-D modeling is accomplished, calculations are performed to obtain the load on the nose gear during landing. Then kinematic analysis is performed and modeling decisions are then made on how to transfer the loads into the finite element

model (FEM). The FEM is then used in predicting the stress behavior during landing. The FEA software used in this analysis is Algor by Autodesk. Figure 1 shows the Twin Otter aircraft with the nose gear and main gear configuration. Figure 2 shows the breakdown of all the components within the nose gear.

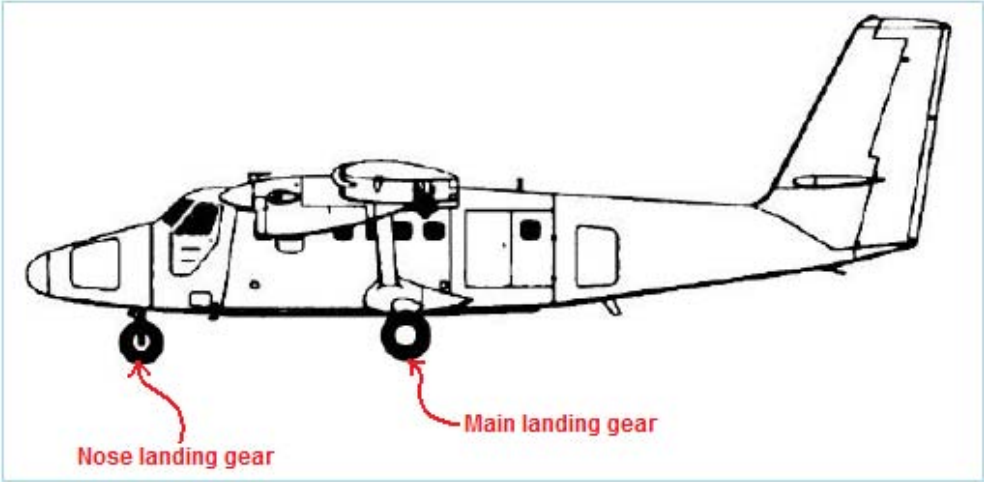


Figure 1: Twin Otter Aircraft showing the locations of landing gears

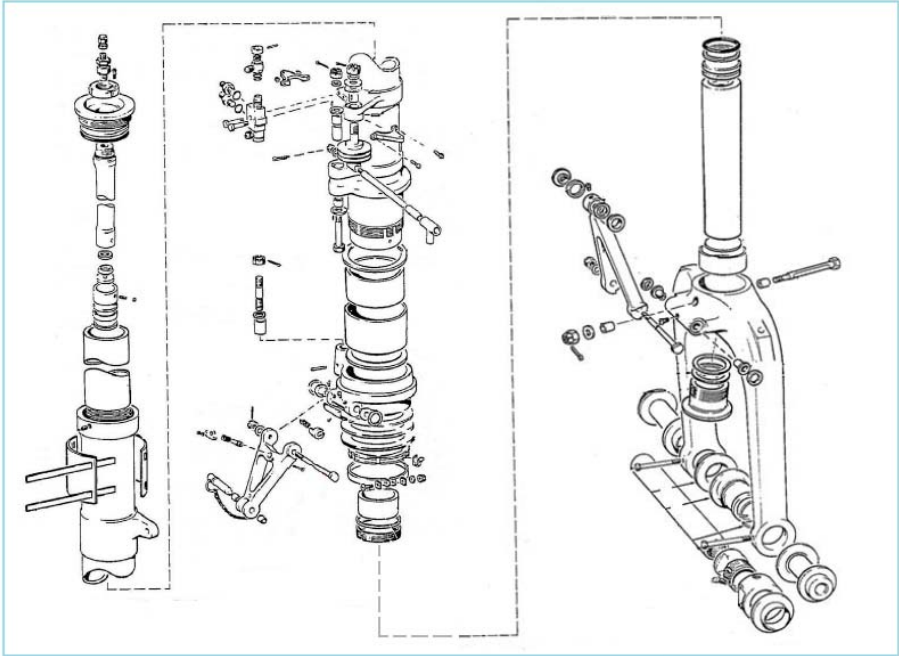


Figure 2: Breakdown of the nose gear

Chapter 2: LITERATURE REVIEW

2.1 Background

The development of finite element analysis was traced back to the 1940s when Courant used the Ritz method of numerical analysis and minimization of variational calculus to approximate vibration systems [3].

Finite element analysis is a tried and trusted method in studying stresses, displacements, fluid flow, vibration and more. It is used early in the design stage to predict the life cycle of a product. Linear static stress analysis is defined as $\{f\} = [K] * \{x\}$. Where $\{f\}$ is the applied load vector, $\{x\}$ is the displacement vector, and $[K]$ is the assemblage of all individual element stiffnesses [4]. Since the individual element stiffness is defined by the user based on the material property, and the applied load is defined based on the application, the only unknown left to calculate is the displacement vector $\{x\}$. Once the displacements and strains are determined, stresses can be obtained using Constitutive equations. Finite element analysis generally breaks down into three processes: the pre-processor, processor, and post-processor. During pre-processing, a CAD model is typically discretized into a mesh, loads and boundary conditions are applied, and material properties are assigned. The next process is to perform the analysis, and finally the post-processor allows the analyst to review, analyze, and record the results.

In this thesis, the nose landing of the Twin Otter aircraft is selected for study. Twin Otter was manufactured by De Havilland Canada. Over 800 aircrafts were built between 1965 and 1988. It was designed with the short takeoff and landing (STOL)

capability. The landing gear configuration is fix tricycle with a main gear and a nose gear. (Refer to Figure 1 for more details). In commercial aviation, aircrafts often are divided into several classifications. For instance, Part 23 Aircraft has the maximum gross landing weight of no more than 12,500 lbs. Part 25 Aircraft has the maximum landing weight beyond 12,500 lbs. Part 27 is for rotorcraft, which has a maximum landing weight of no more than 7000 lbs. Other classifications exist. The Twin Otter aircraft is classified under Part 23 Aircraft because its maximum landing weight is 12,300 lbs.

2.2 Eye-bar Theory

The eye-bar theory is applied in determining how to distribute the ground reaction force on the wheel. To better understand this theory, refer to Figure 3 showing the eye-bar under loading. The eye-bar theory is used to study the method of applying the load directly on the wheel without analyzing the tire. Subsequent sections will describe the contact of the tire and the wheel interface in more detail.

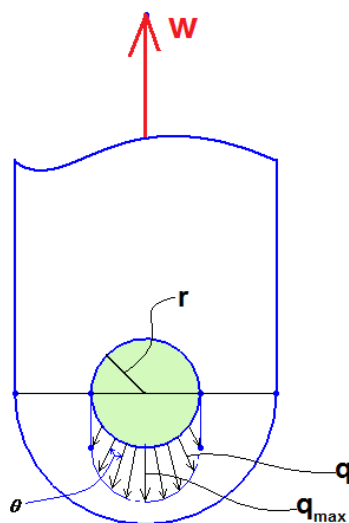


Figure 3: Eye-Bar Loading

From Figure 3, the maximum unit load q_{\max} on the eye-bar can be calculated from equation 2.2.1:

$$W = \int_0^{\frac{\pi}{2}} 2 \cdot r \cdot q \cdot \cos(\theta) d\theta \quad (2.2.1)$$

Where W is the applied load, r is the radius of the pin. After the integration, the result of equation 2.2.1 is $W = \frac{\pi \cdot q_{\max} \cdot r}{2}$.

A similar method can be applied for the tire and wheel interface, where the pressure on the bead seat is calculated based on the ground reaction force on the tire. This eye-bar theory has been applied to tire/wheel interfaces before. For example, Stearns derived the applied pressure (W) at the bead seat region to be as follow:

$$W = \int_{-\theta_o}^{\theta_o} b \cdot W_r \cdot r_b \cdot d\theta \quad (2.2.2)$$

Where $W_r = W_o \cdot \cos\left(\frac{\pi}{2} \cdot \frac{\theta}{\theta_o}\right)$; giving $W = \frac{W_o \cdot 4 \cdot b \cdot r_b \cdot \theta_o}{\pi}$ or $W_o = \frac{W \cdot \pi}{4 \cdot b \cdot r_b \cdot \theta_o}$, where W_o

is the maximum pressure, W_r is the distributive pressure, r_b is the radius of the wheel, b is the width of the bead seat, and θ_o is the contact patch angle.

2.3 Tire/wheel interface

In an effort to not model the tire, the wheel/tire interface has been carefully studied and appropriate loads have been applied to the wheel directly. Similar simplifications of tire/wheels have been used in analysis by other researchers. Many have performed tire/wheel interface analysis to automotive wheels, where the authors study the

stress and displacement of the automotive wheel without modeling and performing the non-linear material analysis of a tire [5], [6].

Stearns used the eye-bar analogy similar to Blake [9] to determine pressure distribution at the contact areas of the tire bead seat and the wheel. Stearns used Algor finite element analysis software to study the stresses and displacements. The analytical results showed a good correlation with the physical testing results. Although Stearns' work focuses on the automotive wheel, the concept is still the same for aircraft wheel. The study of the tire-wheel interface is a continued effort for many tire/wheel manufacturers and researchers in order to meet the goal of continued improvement and quality products.

Kandarpa, Spencer Jr., Schudt, and Kirkner developed a numerical tool to determine the pressure distribution at the tire-wheel interface of an aircraft wheel [7], [8], while Tielking used FEM to determine the tire/pavement pressure distribution [10],[11]. Several strain gauges were used to obtain the strain measurements along the bead seat region. Fourier series and a least square fit to back calculate the pressure exerted by the tire onto the wheel at the tire/wheel interface was used. The computer code ANTWIL was developed to compare the results with the Fourier method.

Another method of calculating the pressure distribution at the tire/wheel interface was studied by Sherwood [12]. Sherwood used piezoelectric film to measure the pressure at the interface. Piezoelectric film was installed along the tire/wheel contact surface. When the pressure was applied, the film started to deform. As the pressure changed, the voltage started to change. The changes in the voltages were calibrated to correlate to the strain. To study the displacement of the tire/wheel interface, Sherwood used holographic

interferometry to take the measurement. This same method was also studied by former researchers. In addition to the experimental results, Sherwood performed a three-dimensional finite element analysis using Adina. Three different methods were analyzed and discussed. FEA at the tire/wheel interface was widely used.

The earlier works from Jeusette and Theves (1992) and Tseng, Pelle, and Chang (1989) used FEA element analysis to study different loading scenarios such as braking, cornering, and the combination of braking and cornering [13], [14]. Tseng, Pelle, and Chang modeled the tire using the nonlinear incompressible elements with the cord-rubber composite element. The finite element analysis approach was divided into three categories as followed: modeling of rubber compounds, modeling of cord-rubber composites and modeling for the gap.

Rubber compound was assumed to have the nonlinear elastic material property without considering viscoelastic characteristics. Young's modulus was determined from the experimental data using $E = 6(C_{10} + C_{01})$ where C_{ij} are material constants. The cord-rubber composite was modeled using orthotropic material. Finally, the gap was modeled to study the tire and wheel at no inflation pressure [15]. In addition to the literature review of the tire/wheel interface described previously, FEM of the tire and wheel analysis were heavily reviewed [16],[18],[30][31].

2.4 Shock absorber

The shock absorber analyzed in this thesis is the most current and modern type of shock absorber available. It provides the highest efficiency in absorbing energy during landing compared to other types of conventional shock absorbers. This type of absorber is

called “oleo-pneumatic.” It works inside an enclosed system where oil and air are being used.

Wang, Xing, Price, and Li (2008) developed the mathematical model to control the vibration caused by landing impacts and runway excitation where the authors described the three forces from the shock absorber similar to those studied in this thesis [35]. A similar method of deriving the shock absorber forces was performed by Dong-Su, Hong-bin, and Hui (2007) [24]. Dong-Su, Hong-bin, and Hui (2007) derived the frictional force as the function of internal pneumatic force and the coefficient of kinetic friction.

Due to the non-linear behavior of the oleo-pneumatic shock absorber, there are many different factors to take into consideration during the design stage to achieve the highest efficiency. Those factors include the total stroke, compression ratio, air and fluid volume [19]. In 1965, the military specification (MIL-L-8552) for the air-oil shock absorber was implemented to require certain materials, protective treatment, process, and efficiency to be used on the oleo-pneumatic shock absorbers.

Many academic institutions, government agencies, and aircraft manufacturers have studied and continued to improve the efficiency of the shock absorber over many years. In addition to the analytical approach of analyzing the shock absorber, Walls performed the experimental study of the internal strut pressure and loads on the small shock absorber [34]. His experiment only focused on a specific range of shock strut velocity and strokes. Walls concluded that the orifice coefficient increased slightly with increasing the velocity for the Reynolds number ranging from 9,500 to 66,500. The change of orifice coefficient due to the chamfer length was very small. Forces from the internal

pressure correlated well with the computation forces from accelerometer and dynamometer measurement.

Another similar work was done by Milwitzky and Cook to study the behavior of the landing gear [20]. The author described the three shock absorber forces more in depth, and similar forces are studied in this thesis. The drop test was performed to compare the analytical to the experimental results. Milwitzky and Cook concluded that both results were to be in good agreement. The method of obtaining the frictional, hydraulic and pneumatic forces from the shock absorber was a proven method to use; therefore, this thesis will use this method to extend the study of those forces.

2.5 Materials

Aluminum and alloy steel are the most common materials used in the nose gear assembly. Aluminum provides a high corrosion resistance property while maintaining the structural integrity to support the aircraft. Some of the parts in the nose gear assembly are forged before the final products are machined.

For this particular aircraft, the fork and the main cylinder are forged while the nose wheel is cast. The benefit of casting is the ability to achieve the complexity in the shape of the part; however during the solidification of the material, porosity, cracks and segregations might develop; therefore the mechanical properties sometimes are not as good as forging.

Due to the limited availability of 2014 aluminum vs. 7075 aluminum, many of the nose gear parts are made using 7075 aluminum as the alternative to 2014. When compared to 2014, 7075 has better mechanical properties and stress corrosion resistance while both materials have approximately the same weight.

Appropriate materials selection during the design stage of the landing gear is very important. A material guideline was created by Curry to assist the designers and engineers when selecting the materials [23]. His guidelines include the inspection method, strength requirement, material samples, hardness, and surface finishes.

2.6 Finite Element Method (FEM)

In 1943, the mathematician Richard Courant published the paper, “Variational methods for the solution of problems of equilibrium and vibrations,” describing the equation for solving torsion problems using the finite element method. His paper was the introduction of the finite element method. Until late 1950s and early 1960s, computer codes were used in the aircraft industry to perform structural analysis, which was similar to what is now called FEA.

In 1965, the Wright-Patterson Air Force Base in Dayton, Ohio, held the first conference with the FEA topic called “Matrix Methods in Structural Mechanics”. Over many decades of implementing for better software, FEA courses are today widely used and taught. The book “What every engineer should know about finite element analysis,” by John Brauer describes the history, development and basic concepts of the FEA. The author describes who, when, what and why FEA was developed, then introduces structural, thermal, electromagnetic and fluid analysis. It is one of the starting points for basic understanding of FEA.

In addition to Brauer’s book, there is much more literature discussing the subject of FEA. The work in this thesis requires the understanding of the aircraft, the simplification of the tire, the modeling method and the shock absorber behavior.

As previously mentioned, Stearns used Algor to study the stress and displacement distribution in the automotive rim [5]. Stearns performed the analysis using axisymmetric element, one-quarter of the wheel, half of the wheel and the full wheel. Hexahedral, brick and wedge elements were chosen. The analysis indicated the half and full model produced exact results.

In addition to Algor, another software, ANTWIL (Analysis of Tire-Wheel Interface Loads), was used for the aircraft wheel analysis. ANTWIL was developed more specifically to the tire/wheel interface application. Other FEA software programs that are similar to Algor include Adina, Abaqus and Nastran.

Although tire analysis is not necessary when studying the stress or displacement of the wheel and other parts of the nose gear, it is worth mentioning that it can be done. Dilley and Wallerstein used MSC/Nastran to predict the tire behavior using a radial tire with three-dimensional shell FEM constructed from two dimensional plate elements [17]. Dilley and Wallerstein used anisotropic plate elements for the plies, BAR elements for the bead, GAP elements for the tread and tread/ground contact and torsion spring for the stiffness of the rubber in the bead region. In 1984, NASA conducted a tire-modeling workshop to explore the area of tire analysis. Many reports related to the tire modeling were presented during the workshop included finite element modeling and analysis of tires by Noor and Andersen [21]. The authors specified different modeling methods such as membrane, laminated, and two-dimensional axisymmetric. A tire contact solution technique by Tielking described a method based on the orthotropic, nonlinear shell elements.

3.0 Modeling overview

Modeling consists of the following steps: CAD modeling, determination of forces, determination of interactions between components, and FEA. This chapter discusses the CAD modeling but focuses on determination of stresses and interactions. Chapter 4 provides a detailed overview of the FEA, and the results and discussion are presented in subsequent chapters.

3.1 Computer Aided Design

More than 100 parts make up the nose gear assembly; however, most of those parts are used during ground operation and do not have any effect to the performance of the nose gear during landing; therefore, they are not included in the present analysis.

Figure 4 shows all six components that are used in the analysis on the left and all the parts within the nose gear on the right. Part identification and material properties for each part can be found in Table 6 and Table 7. SolidWorks was used to create the 3-D models for all the parts before exporting into Algor, the FE software used.

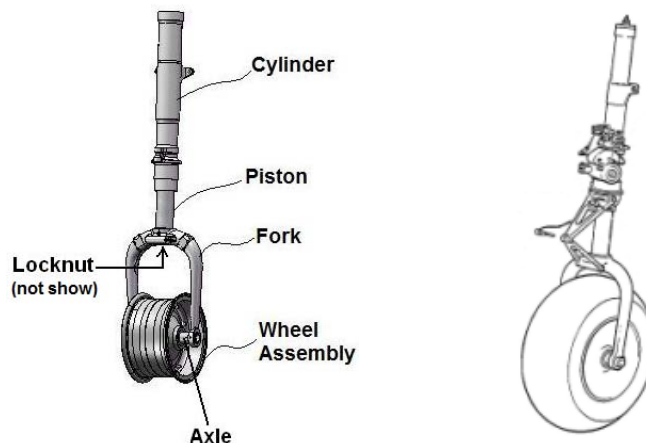


Figure 4: Nose gear parts for FEM Complete Nose gear assembly

A CAD model of the tire was not generated, as there are other ways to model the behavior of the tire on the wheel that do not require non-linear analysis. In this work, the eye-bar theory was applied, as it has been a proven method by the Blake [9] and Stearns [5] where Stearns used it in his automotive analysis. To best approximate the tires behavior on the wheel, the bead seat (the contact surface between the tire and wheel as shown in Figure 7) dimensions of the tire were measured and incorporated into the tire/wheel interface. The inflation pressure from the tire was applied to the wheel all around the wheel as discussed in more detail in section 3.2.1 Ground forces.

3.2 Force Determination

In order to properly analyze the aircraft, a variety of forces needed to be determined. These include the ground forces acting on the tire and how these forces are transferred into the wheel; the forces exerted by the shock absorber, and the inflation pressure applied around the wheel.

3.2.1 Ground forces

The ground reaction force is determined when the aircraft initially makes contact with the runway. The landing configuration is illustrated in Figure 5 where the contact between the nose gear and ground is impending. The linear dimensions a, b, and d were found from the Twin Otter data book and therefore, a', b', and d' (at an incline) could be determined. The center of gravity of the aircraft is shown in Figure 5 at inclined angle to indicate the motion at 1g down and .33g forward [29].

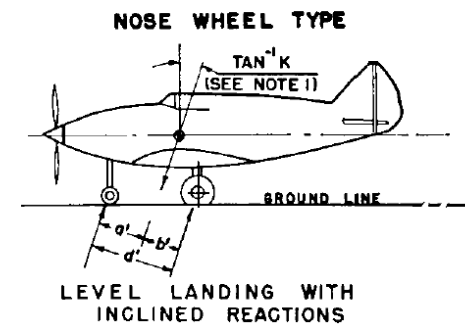


Figure 5: Landing configuration

The dimensional schematic in Figure 6 shows how the dimensions of the nose gear relate to the main gear and the center of gravity.

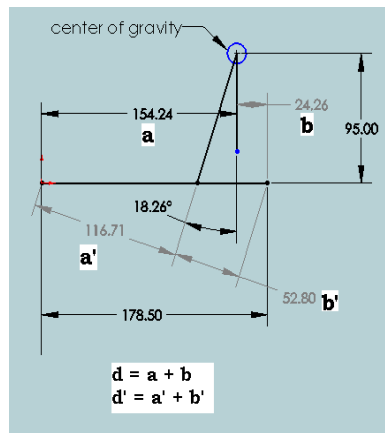


Figure 6: Dimensional Schematic

From Appendix A of Part 23 aircraft, the vertical force at the nose gear is determined as:

$$V_f = (n - L) \cdot W \cdot \left(\frac{b'}{d'} \right) \quad (3.1.1)$$

The maximum weight (W) of the aircraft during landing is 12,300lbs, n represents the ratio of external applied vertical forces to the weight; L is the lift to weight ratio; b' and d' are dimensions defined in Figure 6. Based on equation 3.1.1 and the information obtained from the FAA database [29], the approximate vertical load exerted on the nose gear when the shock absorber is fully compressed at 7664 lbs, computed below.

$$V_f = (2.67 - .67) \cdot 12300 \cdot \left(\frac{52.81}{169.51} \right) = 7664 \cdot lb \quad (3.1.2)$$

The vertical force (V_f) is then converted into pressure using the eye-bar theory to apply at the bead seat location, previously studied by Blake, Sherwood, Tseng and Stearns, and is shown in equation 3.1.3.

$$W_o = \frac{V_f \cdot \pi}{b \cdot r_b \cdot 4 \cdot \alpha} \quad (3.1.3)$$

Where b is the bead seat width, R_b is the radius of the wheel, and α is the patch angle. Another force exerted onto the nose gear of the aircraft is the drag force at the instant following touchdown. At this instant, the wheel does not yet spin. The drag force was determined based on the inertia load factor (n), force at the nose gear, coefficient of friction of the tire and other variations. Drag force is defined in equation 3.1.4.

$$D_f = k \cdot n \cdot W \cdot \left(\frac{b'}{d'} \right) \quad (3.1.4)$$

Where D_f is the drag force, k is the linear variation constant, b' and d' is the distant between the center of gravity to the nose gear and main gear, and W is the maximum weight during landing. Based on the information was obtained from the FAA database and the aircraft manufacturer for the values of k , n , W , b' , and d' , D_f is calculated to be 3376 lbs.

When the wheel assembly starts to rotate, the drag force is calculated based on the kinetic coefficient of friction μ_k and the vertical force V_f . This new drag force is a lot smaller than the drag force during the spin up and spring back. Figure 7 shows a cross-section of the tire/wheel interface.

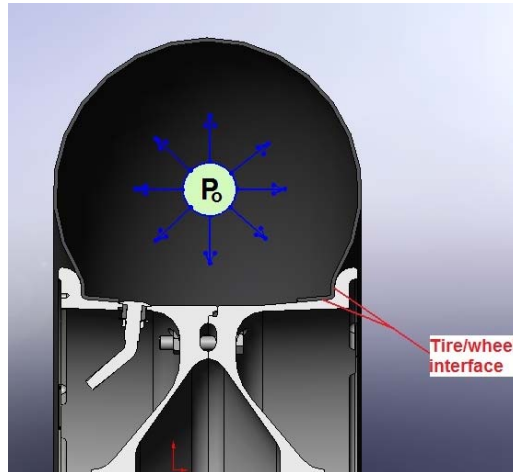


Figure 7: Cross section of tire/wheel

The inflation pressure P_0 , varies only slightly during landing and will therefore be assumed constant. However, the pressure at the tire/wheel interface varies during landing as the reaction force between the ground and tire changes. This pressure will be distributed on the bottom portion of the wheel according to the contact patch region theory. This method was used in previous literatures [12], [27], [5], to describe areas where the wheel will experience the highest pressure during loading. Equation 3.1.5 and Figure 8 can be used to determine the central angle α used to define the contact patch region. Where h is the tire deflection and r is the radius of the tire. These values can be found from the Goodyear tire technical manual [26].

$$\alpha = 2 \cdot \cos^{-1} \left(1 - \frac{h}{r} \right) \quad (3.1.5)$$

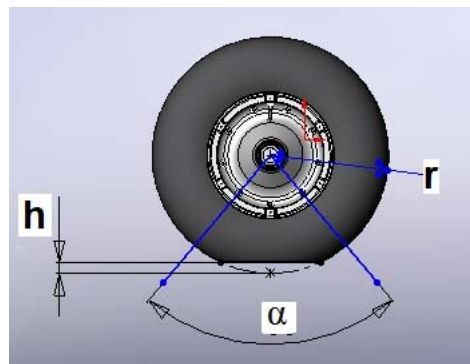


Figure 8: Contact patch region

Once the angle, α , is determined, the load can be applied on the bead seat region along with the inflation pressure around the wheel.

3.2 Shock Absorber forces

An oleo-pneumatic shock absorber is used in the Twin Otter aircraft. This shock absorber consists of pneumatic air is compressed inside the upper portion of the main cylinder. Oleo-pneumatic shock absorbers are used in most modern aircrafts because they provide the highest efficiency of all available shock absorbers. There are two chambers inside the main cylinder of the nose gear. The lower chamber contains MIL-H-5606 hydraulic oil [29], while the upper chamber is filled with compressed air or nitrogen. During the time of the impact, the piston tube is compressed and forces the oil to flow from the lower chamber into the upper chamber (refer to Figure 9). During the compressed stage, hydraulic, pneumatic and friction forces exist. The hydraulics dissipates the energy during landing while the pneumatics provides cushioning during ground operation [33].

A shock absorber is used in the nose gear to absorb and dissipate energy during landing and taxiing. The oleo-pneumatic shock absorber force is a combination of pneumatic force, hydraulic force, and frictional force. When the nose gear is in the air, the shock absorber is fully extended. At the moment when the tire is in contact with the runway, the shock absorber forces start to increase until 100% compression is reached. When the nose gear is fully extended, the only force inside the cylinder is the pneumatic force caused by the initial pressure.

At the fully compressed position, there is an equal and opposite force with the vertical force to prevent the piston from continuing to compress. Figure 9 shows a cross

section of the shock absorber located inside the main cylinder. The right side of the cylinder sees compressed internal pressure at approximately 95 psi. The left side of the cylinder sees the hydraulic fluid. During landing, the piston extends, causing the fluid to flow to the right (up in the application) through an orifice. When the piston extends, the volume inside the cylinder reduces. As a result of decreasing the volume, the internal pressure increases to create pneumatic, hydraulic and frictional forces between the seal and its contact surface.

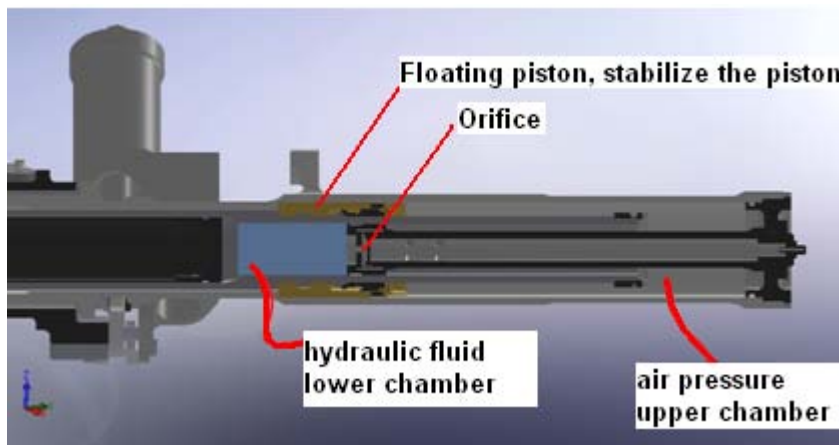


Figure 9: Shock absorber cross section

Pneumatic force

The pneumatic force is the force created when air is compressed under a closed volume. It is determined by the initial air pressure (P_a), the area subjected to the air pressure, and the compression ratio according to the polytropic law for compression of gases $PV^g = \text{Constant}$ or as shown in equation 3.2.1.

$$\frac{P_o}{P_a} = \left(\frac{V_o}{V} \right)^g \quad (3.2.1)$$

Where g is the gas constant and approximately 1.1 [35]. In general, force is defined as the product of pressure and the area on which it acts. Where F_a is the

pneumatic force acting on the piston, A is the cross-sectional area of the piston and remains constant. The new volume V is the difference between the initial volume and the product of the pneumatic area and the stroke. The equation above can be written as:

$$F_a = P_a \cdot A = P_o \left(\frac{V_o}{V} \right)^g \cdot A \quad (3.2.2)$$

Equation 3.2.2 was also derived by [24], [20], [35]. In FEM, either pneumatic pressure or pneumatic force can be applied to the model. In this thesis, pressure is applied to the model. The air pressure from the shock absorber was calculated at 5.5-inch extension and compared with the required value from the Twin Otter maintenance training manual. The result of the calculated value is 144 psi, which fell within the required value from 143 to 147psi. .

Hydraulic force

As the piston tube compresses, the fluid flows through the orifice under compressed air at an initial pressure of 95 psi. As the fluid is forced to flow through the orifice, it creates a hydraulic force. This force is calculated as a function of fluid density (ρ_o), fluid velocity (\dot{y}_s), area of the orifice (A_o), cylinder bore hole (A_h), and coefficient of discharge (C_d) according to equation 3.2.3.

$$F_h = \frac{\rho_o \cdot A_h^3}{2(C_d \cdot A_o)^2} \cdot \dot{y}_s^2 \quad (3.2.3)$$

The surface areas of the orifice and the cylinder bore hole were determined from the CAD models. Fluid density was found using the MIL-H-5606 aircraft fluid specification. The hydraulic force was calculated from values of full extension to full compression. It was determined that the hydraulic force was small compared to the pneumatic force and was therefore not included in the FEA.

Frictional force

The piston tube is supported by the seals located inside of the cylinder. During landing operation, the piston tube compresses from fully extended to fully compressed. The frictional force is caused by the contact between the seals and the piston tube. There are two frictional forces acting on the piston tube. As seen in Figure 10, one occurs at the mating contact between the seal and the upper piston tube (upper normal force N_1) and the other between the cylinder bearing and the lower piston tube (lower normal force N_2). The coefficient of frictions, μ_1 and μ_2 , are depended on the contact surface between the seal and piston tube and between the cylinder and the piston tube. Since both seals have the same material properties and in contact with the same surfaces, the coefficient of frictions and the normal forces can be assumed to be the same.

The frictional force is calculated as the product of coefficient of friction and the normal force. Here, the total frictional force is the sum of the frictional forces caused by each of the two normal forces shown in equation 3.2.4. This equation was also derived by [23], [24], [35].

$$F_f = \mu_1 |N_1| + \mu_2 |N_2| \quad (3.2.4)$$

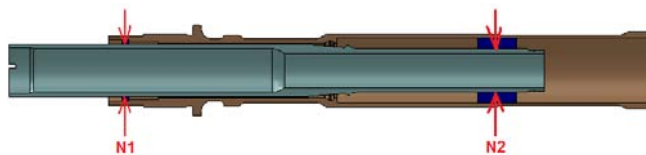


Figure 10: Frictional force from seals

Chapter 4: FINITE ELEMENT ANALYSIS

Having determined the forces acting on the nose landing gear and having created CAD models of the critical components, a finite element (FE) model was developed and analyzed. In developing the FE model, boundary conditions, contact conditions, loads, materials properties, and the mesh were defined.

4.0 Boundary conditions

Boundary conditions are applied to model what is not included in the analysis. As such, boundary conditions were applied where the nose gear is connected to the bulkhead of the aircraft. This connection consists of two bolts and a protrusion between the mounting holes, as seen in Figure 11. The protrusion is used as the anti-rotation feature. This connection is modeled by applying boundary conditions on the circular surfaces of the bolt holes and the protrusion. All degrees of freedom were removed at these boundary conditions, making it fixed. In Algor, there are several options that can be selected from the boundary condition windows, seen in Figure 12.

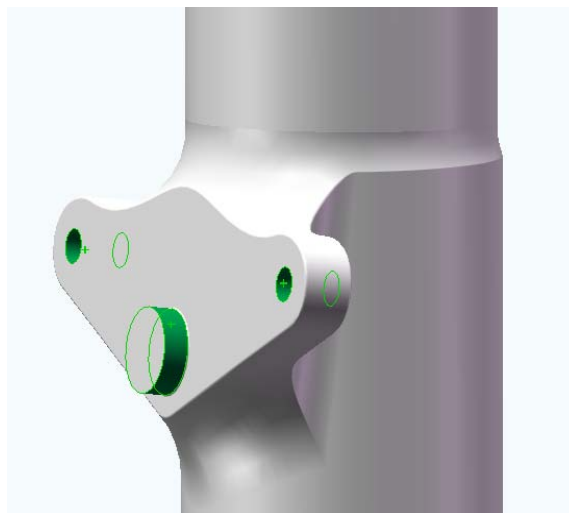


Figure 11: Fixed boundary condition at highlighted surfaces

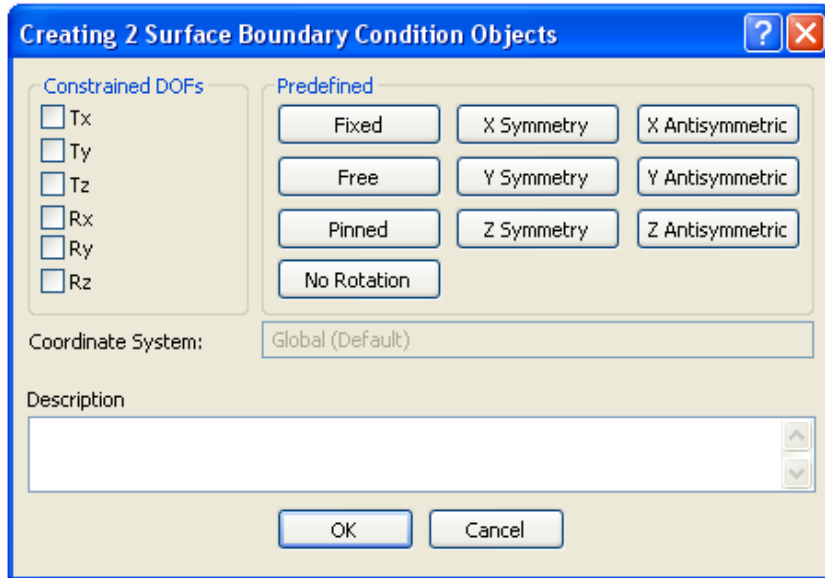


Figure 12: Boundary Condition

This figure shows different options that can be selected base on the application of the parts. The first three constraints on the left side, T_x , T_y , and T_z , indicate translational constraints, whereas R_x , R_y , and R_z indicate the rotational constraints. Table 1 shows other possible boundary conditions, and the degrees of freedom that they remove are indicated with an “x” in the appropriate cell.

	T_x	T_y	T_z	R_x	R_y	R_z
Fixed	x	x	x	x	x	x
Pinned	x	x	x			
No Rotation				x	x	x
X symmetry	x				x	x
Y symmetry		x		x		x
Z symmetry			x	x	x	
X antisymmetric			x	x	x	
Y antisymmetric	x		x		x	
Z antisymmetric	x	x				x

Table 1: Boundary Conditions

4.1 Contacts

One way to transfer forces or pressures from one part to another in the FE model is to model the contact surface between the parts. In this analysis, contacts were modeled at various locations. The coefficients of frictions were obtained from the bearing and seal manufacturers. Different types of contacts can be modeled as shown in Table 2.

Type of Contact	When to use
Bonded/Welded	<ol style="list-style-type: none"> 1. Two surfaces will be in perfect contact 2. Loads are transmitted from one part to another 3. One node on a surface deflects, the node on adjoining surface will deflect
Free/No contact	<ol style="list-style-type: none"> 1. Nodes on two surfaces will not be collapsed to one node 2. Nodes will not transmit loads between parts 3. Nodes will be free to move relative to nodes on other surfaces
Surface contact	<ol style="list-style-type: none"> 1. Nodes will be free to move away from each other but cannot pass through each other when they contact 2. Friction can be added 3. Commonly use for rotation or allowing relative motion between objects
Edge contact	<ol style="list-style-type: none"> 1. Nodes from one edge will move relative to nodes from the other edge 2. Similar to surface contact but applied to edges

Table 2: Uses of each contact in linear static stress

Figure 13 shows how contact is chosen in the software.

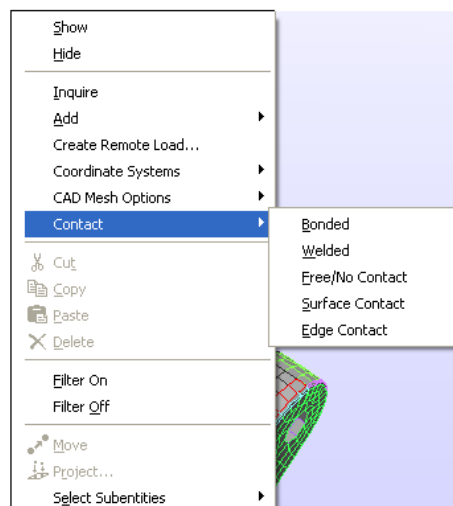


Figure 13: Contacts options

For the present analysis only surface contact and bonded were used. All connections between 3-D CAD components in this thesis were modeled using exact-fit dimensions where no gap occurs between the components. For example, the hole diameter is the same as the bolt diameter. Table 3 shows all contact connections and how they were modeled.

Surfaces	Contact	Coefficient of friction	Comments
Fork/axle	bonded	N/A	Axle is bolted into the fork to prevent it from rotating
Wheel/axle	Surface/surface	0.0018 [32]	Wheels rotate about the axle
Locknut/fork	bonded	N/A	Locknut is mounted onto the fork to hold the piston
Locknut/piston	bonded	N/A	Locknut prevents the piston from coming loose
Bearing/piston	Surface/surface	0.04 [28]	Piston slides up/down during ground, take-off and landing operations
Bearing/cylinder	bonded	N/A	Bearing is pressed fit into the cylinder's inside diameter to hold the piston and to allow it to extend/retract

Table 3: Contact surfaces

4.2 Loading

Three different loading conditions are applied to the nose gear. They are the inflation pressure, ground vertical force, horizontal forces (due to spin up and spring back drag), and shock absorber forces. The vertical force is applied based on the eye-bar theory and using the tire/wheel interface. The inflation pressure is applied 360 degrees around the wheel. The shock absorber force is applied at the top of the piston with a downward force and applied to the top of the cylinder in the opposite direction.

Figure 14 shows how the inflation pressure applied around the wheel.

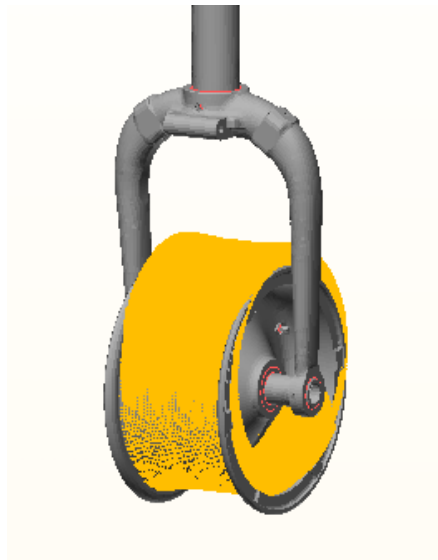


Figure 14: Inflation pressure distribution around the wheel

The inflation pressure around the wheel was assumed to remain constant since the change of the tire volume is minimal during landing.



Figure 15: Bead seat pressure caused by vertical force

The vertical force at the tire/wheel interface is applied based on the eye-bar theory and the contact patch region theory discussed in section 3.2.1. The spin up and spring back horizontal force (D_f) is applied into the FE model using the remote load. Remote load is the method of applying the load at the point that does not exist in the model. In this thesis, it is the point where the tire contacts the runway (since the tire is not part of the analysis). When applying the remote load, line element is used to connect the point in

space (point of the tire/runway) back into the model to allow the load to transfer into the model without adding stiffness to the assembly. The drag force is applied in the x direction parallel to the ground. Figure 16 illustrates the drag force and all the stiffness elements connected onto the tire/wheel interface region.

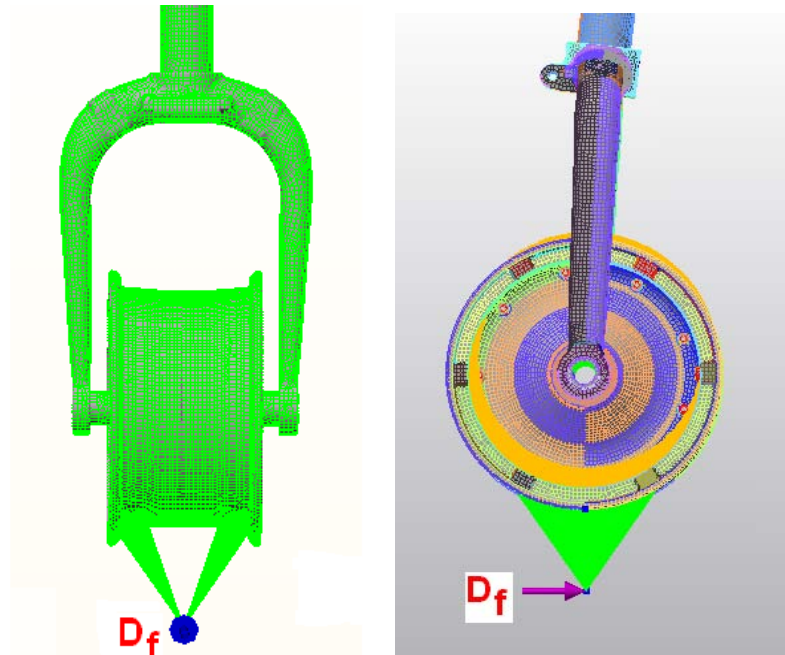


Figure 16: Drag force at the point of contact with ground

The shock absorber forces consist of frictional forces and pneumatic and hydraulic forces. The frictional force component was modeled using contact surfaces, as described in section 3.2. The hydraulic force is small and not include in the model. The pneumatic pressure is applied onto the top surfaces of the piston and cylinder as shown in Figure 17.

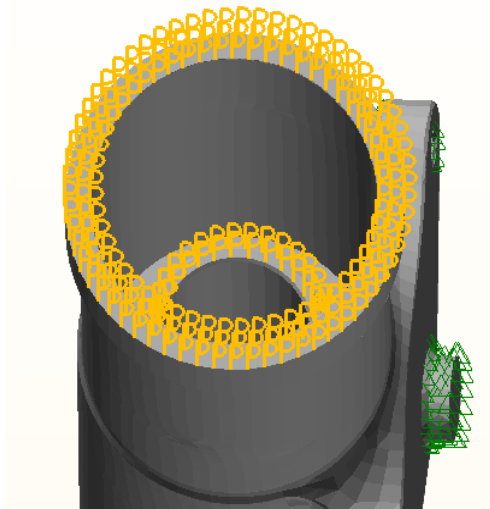


Figure 17: Shock absorber force at piston

4.3 Meshing

There are many different types of meshing options that can be used for the FE model. A list of element types available in Algor and when to use them can be found in Table 4.

Element type	When to use
Truss	<ol style="list-style-type: none"> 1. Length is appx. 8-10 times greater than width and depth 2. External applied forces only at joints 3. Connected to the rest of the model with hinges that do not transfer moments
Beam	<ol style="list-style-type: none"> 1. Element has constant cross-sectional properties 2. Length is much greater than width or depth 3. Element must be able to transfer moments
Membrane	<ol style="list-style-type: none"> 1. Thickness of the element is very small compared to length and width 2. Element will have no stress in the direction normal to the thickness 3. Element does not carry or transmit any moments
Brick	<ol style="list-style-type: none"> 1. Model only allow forces (no moments) 2. Hydrostatic pressure load is allowed 3. Stress results through thickness of a part are needed
Plate	<ol style="list-style-type: none"> 1. Thickness is small (appx. 1/10 to length and width) 2. Small displacement and rotation 3. Elements remain planar, no warping 4. Stress distribution through thickness is linear

Tetrahedron	<ol style="list-style-type: none"> 1. Model only allow forces (no moments) 2. Hydrostatic pressure load allowed 3. Stress results through thickness of a part
Spring	<ol style="list-style-type: none"> 1. Two parts are connected by a spring with a known stiffness value 2. Two part are connected by a part that will only transmit an axial force
Rigid	<ol style="list-style-type: none"> 1. Two parts are connected by rigid connection 2. Model the effect of a part without modeling the entire part
Gap	<ol style="list-style-type: none"> 1. To determine contact force between two parts under load 2. To model effects of spring or cable when stiffness is not present
Thin Composite	<ol style="list-style-type: none"> 1. Model by many thin layers 2. Length and width at least 5 to 10 times the thickness 3. Elements are initially flat
Thick Composite	<ol style="list-style-type: none"> 1. Model by layers with 1 layer much thicker than others 2. Length and width at least 2 to 3 times the thickness 3. Elements are initially flat

Table 4: Element Descriptions

Based on the shape and geometry of all parts in the nose gear assembly, brick, tetrahedral and wedge elements are the most appropriate for this application. The size of the elements ranges from 10% to 150%, where 100% is considered as the nominal or default mesh size. Algor has the capability to automatically re-mesh the model if it is determined that the model has water tightness problems (missing edges), negative Jacobian or other meshing incompatibilities. The number of iterations and the mesh size reductions can be defined by the user. A convergence check was performed by meshing the models with different size elements until the stress converged.

Table 5 indicates the total number of elements and element types used in modeling each component. Brick element was chosen for the analysis, but since element types such as tetrahedral elements, pyramids, and wedges were toggled on inside the mesh engine, the meshing routine chose the most appropriate combination of these elements in meshing the components. Figure 18 shows some of the examples of different

types of solid elements. The resulting model was dominated by tetrahedral and pyramid elements.

Part numbers	Part descriptions	Tetrahedral	Pyramids	Wedges	Bricks	Number of elements
71-111-15	Nose cylinder	42659	17911	1641	6150	68361
71-136-9	Fork	48978	12433	3050	9070	73531
71-141-9	Piston Tube	18299	11357	734	5100	35490
71-156-11	Lock nut	5523	1737	304	557	8121
3-1197	Nose wheel assym. (both wheel half)	104783	29802	5621	14909	155115
71-135-3	Axle	5230	3176	504	1101	10011

Table 5: Element types and quantities

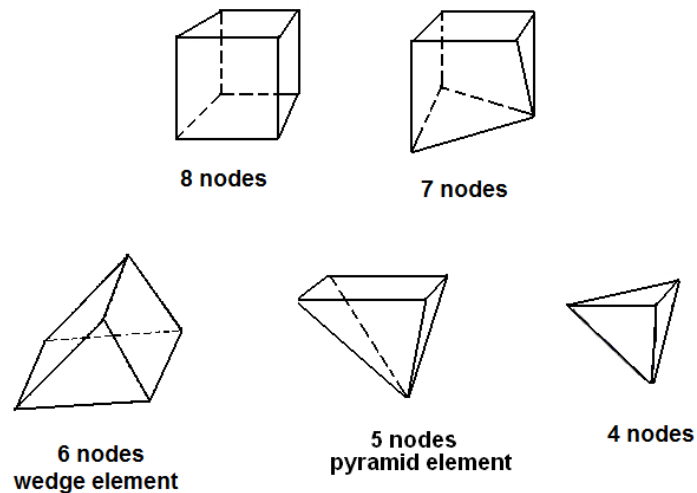


Figure 18: Different types of brick element

Figure 19 shows the final mesh of the nose gear. Match meshing (ensuring that the nodes of one component are matched with the nodes of a mating component) is very essential in FEM, especially when setting up the contact to be surface to surface.



Figure 19: Nose gear mesh

There are several locations within the nose gear that requires surface-to-surface contact as described in Section 4.1. Figure 20 shows how the seal and piston meshes are matched.

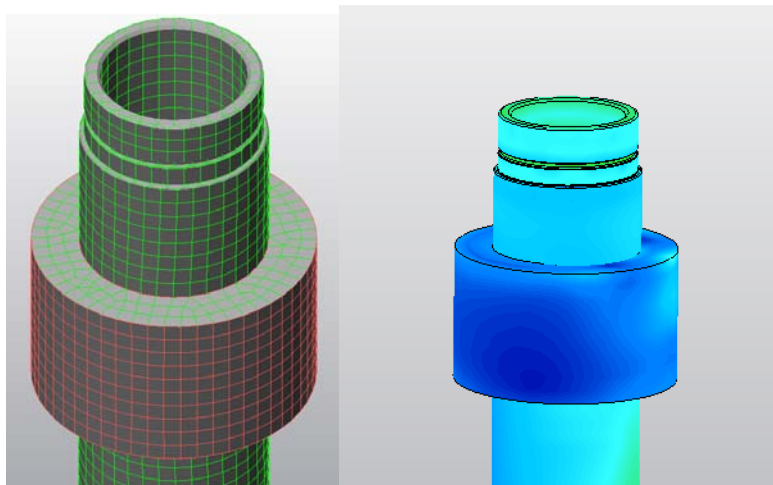


Figure 20: Surface matching

Each element from the seal is matching well with each element from the piston to allow the piston to move as the force is applied. If surfaces from the seal and the piston do not match, the piston can move through the seal. Figure 21 shows an example of

surfaces not matching. This causes loads to be transferred incorrectly and components to separate from each other.

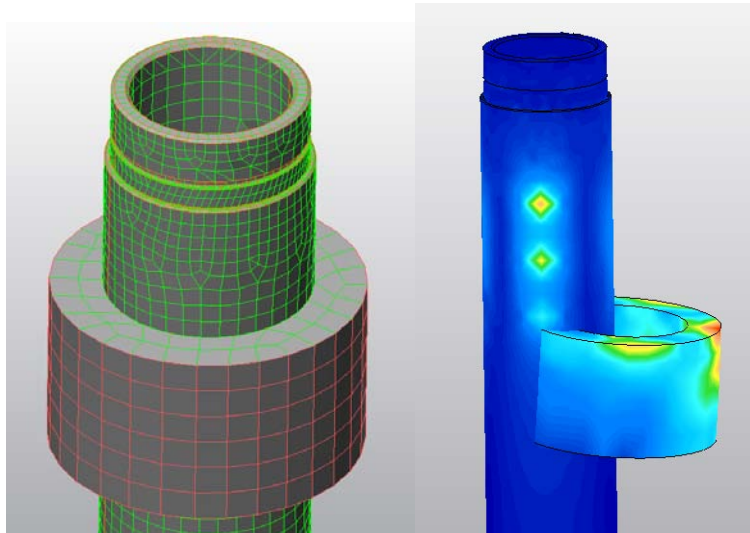


Figure 21: Surface not matching

In FEM, the finer the mesh, the longer it will take to compute the results. The accuracy of the results will increase as the mesh is refined up to the point of mesh convergence. To ensure the mesh is fine enough but not too time expensive, a convergence study was performed. The process of performing a convergence study is to mesh the model with a certain number of elements and analyze the results, such as stress. Then refine the mesh and re-analyze the result process several times. The stress values are then plotted as a function of element size. If increasing the number of elements do not change the stress values significantly, the mesh can be considered converged.

4.4 Material selection

There are many different types of materials used in the nose gear assembly. Table 6 lists all the components and their materials. Table 7 lists some of the material properties

used in the analysis. This table will also be used to help determine if the parts will reach the yield point during the impact.

Part numbers	Part descriptions	Materials
71-111-15	Nose cylinder	7075-T6 Aluminum
71-136-9	Fork	7075-T6 Aluminum
71-141-9	Piston Tube	4340 Steel
71-156-11	Lock nut	4340 Steel
3-1197	Nose wheel assy.	AZ91C Magnesium alloy
71-135-3	Axle	4340 Steel

Table 6: Material Identification

	7075-T6	4340 Steel (Normalized)	AZ91C - T6
Ultimate tensile strength (ksi)	83	177	39.9
Yield strength (ksi)	73	114	21
Modulus of Elasticity (ksi)	10400	29700	6500
Poisson's Ratio	0.33	0.290	0.350
Density (lb/in ³)	0.102	0.284	0.065

Table 7: Material Properties

Chapter 5: RESULTS

All of the essential parts from the nose gear as described from the previous sections were analyzed. It took about four hours to run the analysis. The results indicated the maximum stress occurs in the wheel assembly, specifically at the area where the loads are applied as shown in Figure 22. The red color indicates the area of high stress concentration. Figure 23 shows the stress and displacement contours of the nose landing gear. Table 8 indicates the maximum stress and displacement levels in the components analyzed. The calculated stress values were compared with the ultimate tensile strength of the respective material to estimate the factor of safety. Per FAA requirement on physical testing, the nose wheel assembly has to meet a minimum factor of safety of 2.0 for cast materials. The analysis resulted in a minimum factor of safety of 3.0 at the wheel, well within the FAA's requirements.

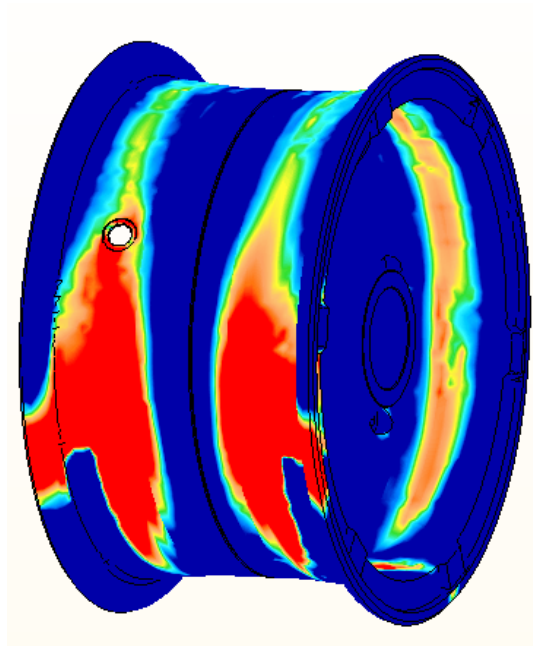


Figure 22: Wheel assembly - stress concentration

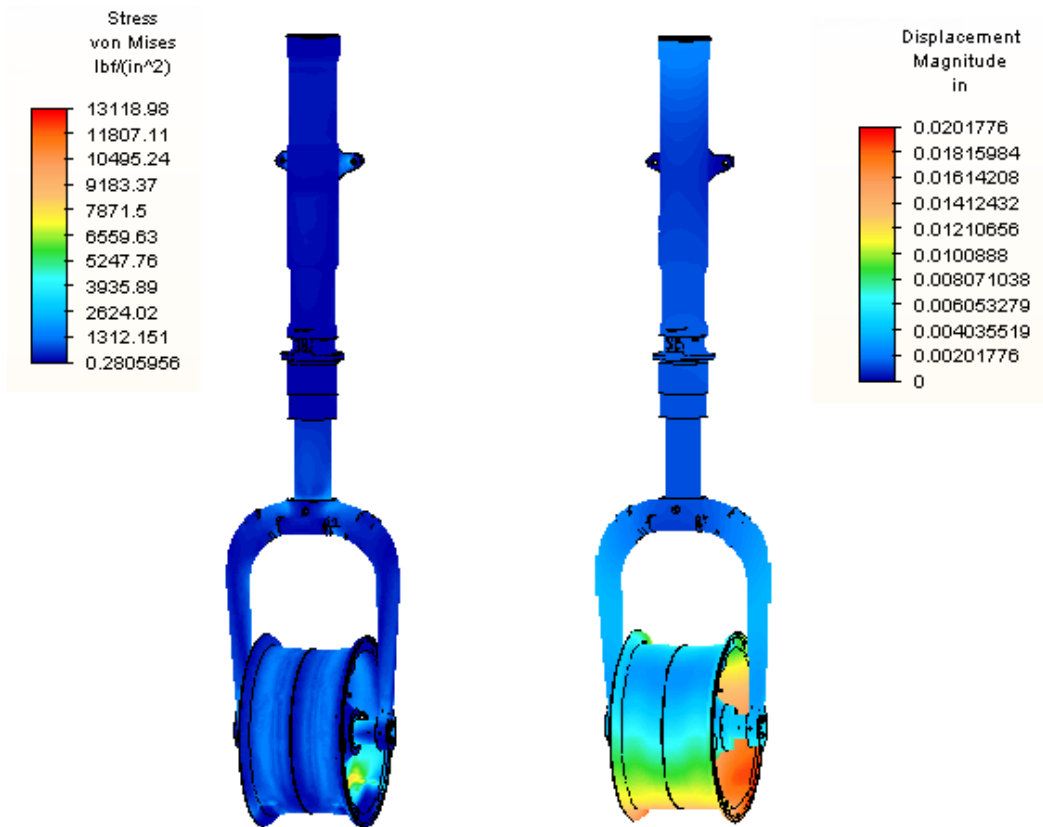


Figure 23: Stress and Displacement

The wheel assembly also yields the largest displacement. This displacement is the deformation of the material and does not include any rigid body motion occurring during landing.

Part numbers	Part descriptions	Stress (psi)	Displacement (in)
71-111-15	Nose cylinder	4179.9	.0030
71-136-9	Fork	3746.0	.0071
71-141-9	Piston Tube	3385.0	.0016
71-156-11	Lock nut	4238.8	.0014
3-1197	Nose wheel assym.	13119.0	.0202
71-135-3	Axle	5609.02	.0077

Table 8: Stress and Displacement results

The stress and displacement plot of the nose cylinder is shown in Figure 24. The results indicate the maximum stress location for this part is at the location of the boundary condition. The material displacement of 0.0025 inches at the top of the cylinder is due to the shock absorber force and the relatively large displacements at the lower portion of the cylinder and due to the compression force from the piston tube.

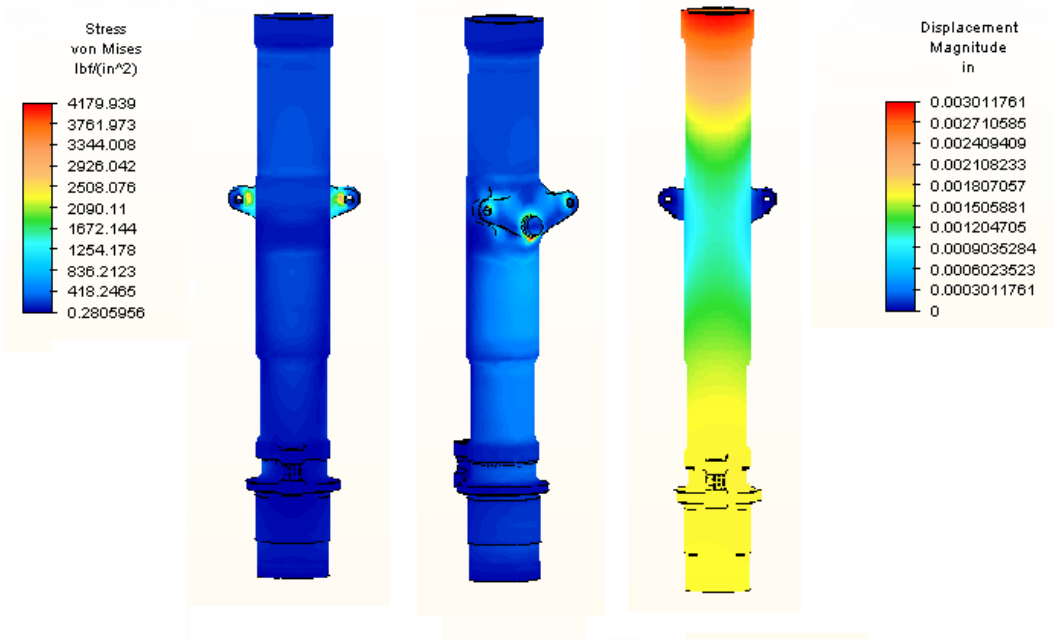


Figure 24: Stress and Displacement of the cylinder

The stress results of the fork are shown in Figure 25. The magnitude of the maximum stress is similar to those found in the cylinder. The maximum stress occurs at the filleted regions directly above the axle mounting location and occurs on both sides of the symmetry plane. The maximum displacement of the material occurs at the axle mounting location, as shown in Figure 25.

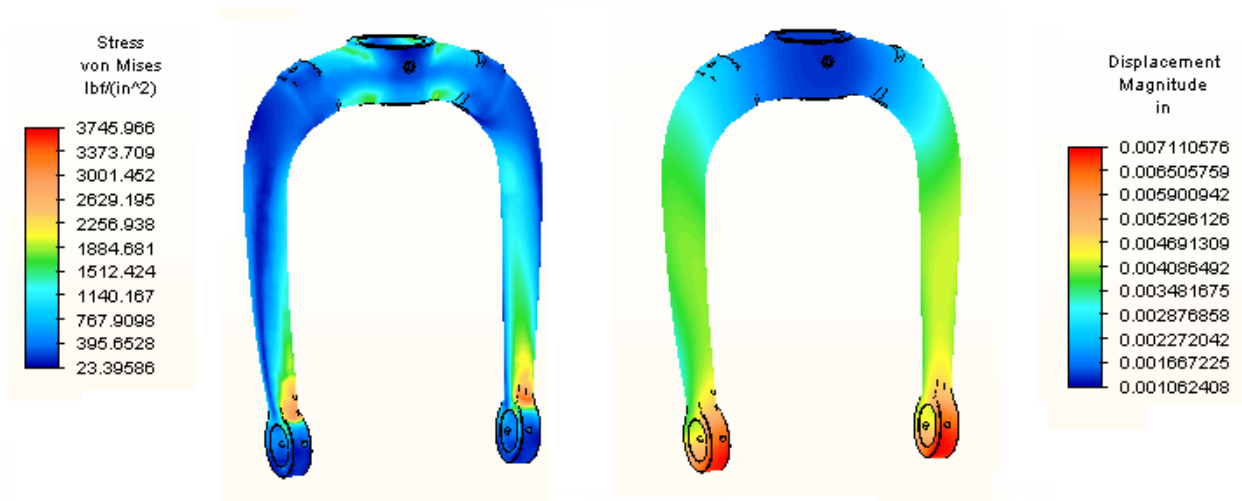


Figure 25: Stress and Displacement of the fork

The factor of safety as shown in Table 9 is determined based on the calculated stress and the maximum stress of the material when the materials start to fail. Table 9 clearly shows that the wheel assembly has the lowest factor of safety compares to all other parts.

Part Descriptions	Calculated Stress	UTS	Factor of Safety
Nose cylinder	4179.9	83,000	19.9
Fork	3746.0	83,000	22.2
Piston Tube	3385.0	177,000	52.3
Lock nut	4238.8	177,000	41.8
Nose wheel assym.	13119	39,900	3.0
Axle	5609.02	177,000	31.6

Table 9: Factors of Safety

Figure 26 shows the stress and displacement distribution in the wheel. From this figure, it is clear that the highest stress is located at the contact patch region of the tire/wheel interface. Displacement is largest at the contact patch region. The large displacements at this region are explained by the large forces applied here and the fact that the boundary conditions are located far away.

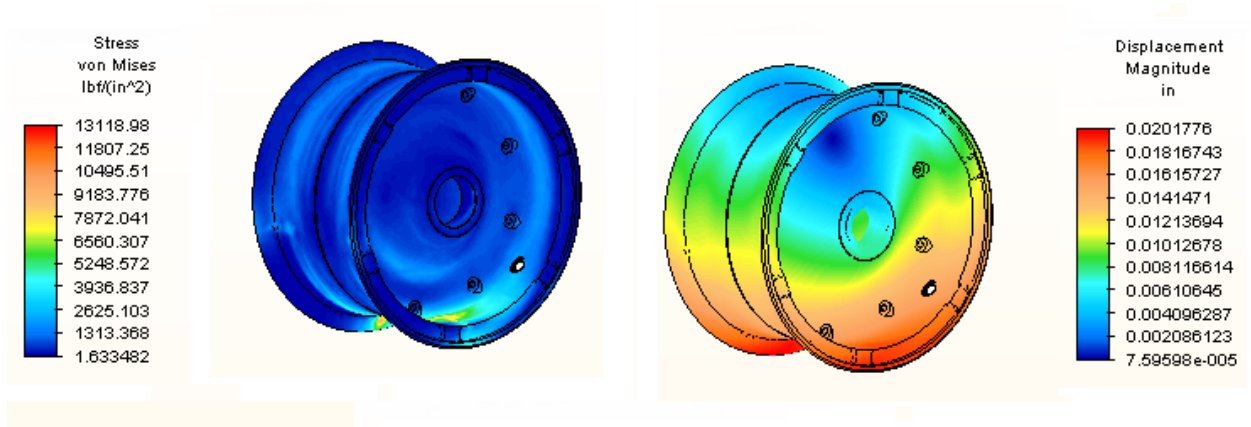


Figure 26: Stress and displacement of the wheel assembly

The piston tube, axle and locknut are shown in Figure 27. All three parts have low stresses and high factors of safety. One thing similar between the piston tube and the axle is that maximum stresses occur at the bearing contact locations since this is where the components experience restrictions and since this is where the forces are transferred into the components.

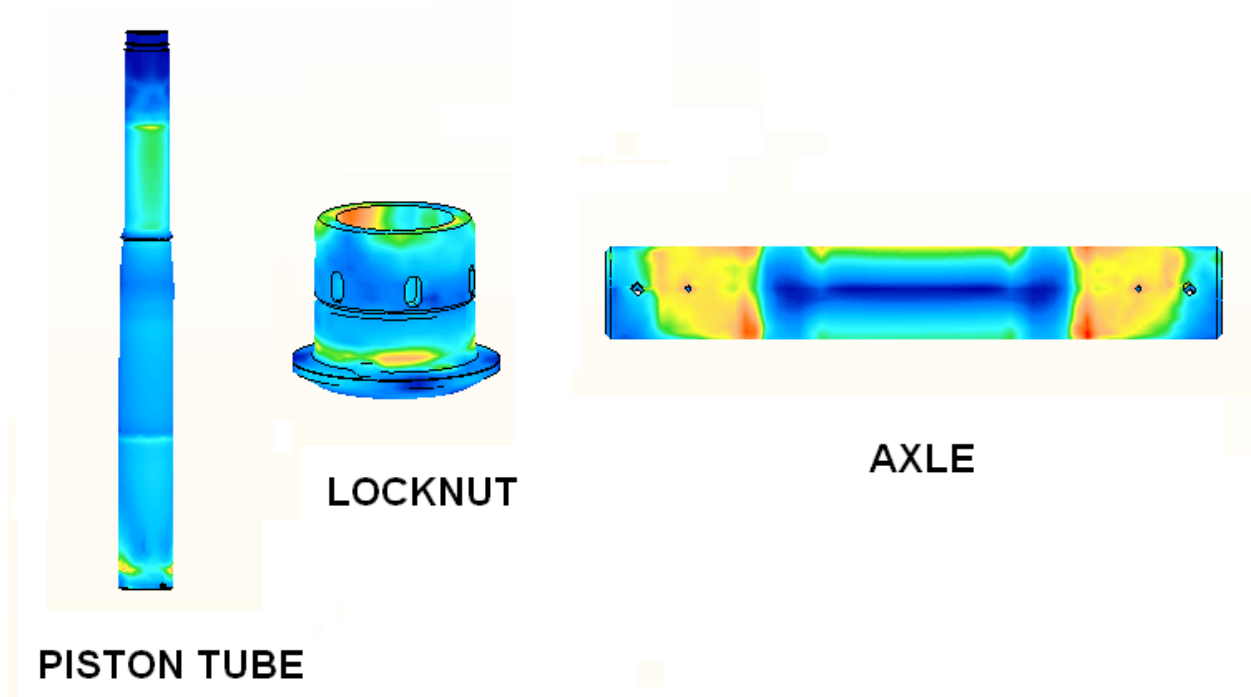


Figure 27: Stress results of the piston tube, locknut and axle

Due to the proprietary information and limited number of publications on the results of the physical testing of the nose landing gear, a side-by-side comparison of the results from this thesis and the previous work is not readily available. However, the similar analysis performed for the automotive wheel is used for comparison. The result for the displacement of the automotive wheel can reach up to 0.28mm [5] and can be compared to the result in this thesis where the wheel displaced 0.51mm. The stress of the automotive wheel gets up to 3190psi compares to 13119psi from this thesis. The stress from the aircraft wheel is much higher than the automotive wheel due the higher applied forces. In addition, the material used on the Twin Otter aircraft is magnesium vs. aluminum in the automotive wheel analysis.

The results obtained for the wheel assembly are acceptable because the 3-D model was generated from an approved wheel data, which had the factor of safety above 2.0. The methods used to simplify the model are proven methods such as modeling the wheel without the tire. All formulas are used in this thesis to determine the forces were from Federal Aviation Administration. The methods of applying the boundary conditions and constraints are based on the application of the nose wheel assembly along with literature reviews.

Chapter 6: DISCUSSION AND CONCLUSIONS

This thesis demonstrated several important factors in analyzing a nose landing gear. First, the function of the nose landing gears must be understood. Second, the time at which the worst case loading scenarios occurs must be determined. For this analysis, this worst case was found to occur directly following impact, and this scenario was selected and analyzed. Third, proper boundary conditions, constraints, and loads must properly be determined and modeled. Lastly, the results obtained must be studied in detail to determine their validity.

This analysis shows that finite element analysis can help manufacturers determine if their designs are safe prior to performing physical testing. FE analysis will allow them to make design alterations prior to manufacturing and testing, which in turn can save them time and money. This analysis was performed on the Twin Otter nose landing gear, but similar analysis can be performed on other landing gears to help predict failure.

Future research can be implemented from this thesis, such as incorporating the tire into the analysis, performing non-linear and dynamics stress analysis at the time the tire contacts with the runway until the aircraft stop, and performing physical testing for validation purposes.

REFERENCES

1. Hootman J.A, Jones A.R. Results of Landing tests of various airplanes. Langley Memorial Aeronautical Laboratory, 1942
2. FAA. 2009. <<http://av-info.faa.gov/sdrx/Query.aspx>>.
3. Courant, R. "Variational methods for the solution of problems of equilibrium and vibrations." Bulletin of the American Mathematic Society 49.1 (1943): 1-23.
4. Cook, Robert D. Finite element modeling for stress analysis. Madison: John Wiley and Sons, Inc., 1995.
5. Stearns, John C. An Investigation of stress and displacement distribution in a aluminum alloy automobile rim. Akron: University of Akron, 2000.
6. Ridha, R A. "Finite element stress analysis of automotive wheels." Automotive engineering congress and exposition (1976).
7. Kandarpa, S, B F Spencer Jr. and D J Kirkner. "Determination of tire-wheel interface loads for aircraft wheels." Journal of Aircraft 31. No. 2 (1994).
8. Schudt, E E, et al. "Three-Dimensional verification of an axisymmetric algorithm for tire-wheel interface load recovery." Aerospace Atlantic Conference and Exposition. Dayton: Society of automotive engineers, 1994.
9. Blake, A. Practical stress analysis in engineering design. McGraw-Hill, 1990.
10. Tielking, John T. "A tire contact solution technique." n.d.
11. "Aircraft tire/pavement distributions." Aerospace technology conference and exposition. Anaheim: Society of Automotive Engineers, 1989.
12. Sherwood, J A, et al. "An Investigation of tire-wheel interface loads using Adina." Computers and Structures (1995): 377-387.
13. Jeusette, J P and M Theves. "Finite element analysis of tire/rim interface forces under braking and corner loads." TSTCA. Tire Science and Technology, 1992. 83-105.
14. Tseng, N T, R G Pelle and J P Chang. "Finite element simulation of tire-rim interface." TSTCA. Tire Science and Technology, 1989. 305-325.
15. Oden, J T, et al. "Finite element methods for nonlinear elastostatic problems in rubber elasticity." n.d.

16. Spencer, B F, et al. "Aircraft wheel life assessment." government report. University of Notre Dame, 1993.
17. Dilley, G A and D V Wallerstein. "Finite element analysis and the modeling of tires." MSC World User's Conference. 1984.
18. Kim, Kyun O, Ahmed K Noor and John A Tanner. "Modeling and analysis of the space shuttle nose gear tire with semianalytic finite elements." NASA technical paper. 1990.
19. Mason, William H and Sony T Chai. "Landing gear intergration in aircraft conceptual design." Research topic support by NASA Ames Research Center. 1996.
20. Milwitzky, Benjamin and Frances E Cook. "Analysis of landing gear behavior." n.d.
21. Noor, Ahmed K and C M Andersen. "Finite element modeling and analysis of tires." NASA conference publication. n.d.
22. J. Mackerle. "Some remarks on progress with finite elements." 55.6 (1995): 1101-1106.
23. Curry, Norman S. Aircraft landing gear design: Principles and practices. Washington: American Institute of Aeronautics and Astronautics, Inc., 1988.
24. Dong-Su, Wu, Gu Hong-bin and Liu Hui. "GA-based bodel predictive control of semi-active landing gear." Chinese Journal of Aeronautics (2007): 47-54.
25. Seth Russell Anthony, Jr. Landing gear loads analysis. Wichita: Wichita State University, 1964.
26. Aviation, Goodyear. Aircraft Tire Data Book. Akron, 10, 2002.
27. Sherwood, James A, et al. "Study of the pressure distribution on an aircraft tire-wheel interface." Journal of Aircraft 32.5 (n.d.).
28. Kamatics . <<http://www.kamatics.com>>.
29. CFR. FAA title 14, part 23. <http://ecfr.gpoaccess.gov/cgi/t/text/text-idx?c=ecfr&tpl=/ecfrbrowse/Title14/14cfr23_main_02.tpl>.
30. Fish, Bradley E, Joseph J Pajot and Delbert K Patterson. "FEA cyclic symmetric fatigue analysis of aircraft wheels." World aviation congress and display. Phoenix: Society of Automotive Engineers, 2002.

31. Flugrad, Donald R and Bruce A Miller. "Experimental and finite element study of a standing torus under normal and tangential loads." n.d.
32. Timken bearings. <<http://www.timken.com>>.
33. Jack, Pink. "Structural integrity of landing gears." Tanner, John A, et al. Emerging technologies in aircraft landing gear. Warrendale: Society of automotive engineers, 1997. 3-14.
34. Walls, James H. An experimental study of orifice coefficients, internal strut pressures, and loads on a small oleo-pneumatic shock strut. National advisory committee for aeronautics. Langley Field: Langley Aeronautical Laboratory, 1955.
35. Wang, Haitao, et al. "An investigation of an active landing gear system to reduce aircraft vibrations caused by landing impacts and runway excitations." *Journal of Sound and Vibration*. 2008.

APPENDIX A

Basic Landing Conditions

Condition	Nose wheel type		
	Level landing with inclined reactions	Level landing with nose wheel just clear of ground	Tail-down landing
Reference section	23.479(a)(2)(i)	23.479(a)(2)(ii)	23.481(a)(2) and (b).
Vertical component at c. g	nW	nW	nW .
Fore and aft component at c. g	KnW	KnW	0.
Lateral component in either direction at c. g	0	0	0.
Shock absorber extension (hydraulic shock absorber)	Note (2)	Note (2)	Note (2).
Shock absorber deflection (rubber or spring shock absorber), percent	100	100	100.
Tire deflection	Static	Static	Static.
Main wheel loads (both wheels) (Vr)	$(n-L) W a'/d'$	$(n-L) W$	$(n-L) W$.
Main wheel loads (both wheels) (Dr)	$KnW a'/d'$	KnW	0.
Tail (nose) wheel loads (Vf)	$(n-L) W b'/d'$	0	0.
Tail (nose) wheel loads (Df)	$KnW b'/d'$	0	0.
Notes	(1)	(1), (3), and (4)	(3) and (4).

Note (1). K may be determined as follows: $K=0.25$ for $W=3,000$ pounds or less; $K=0.33$ for $W=6,000$ pounds or greater, with linear variation of K between these weights.

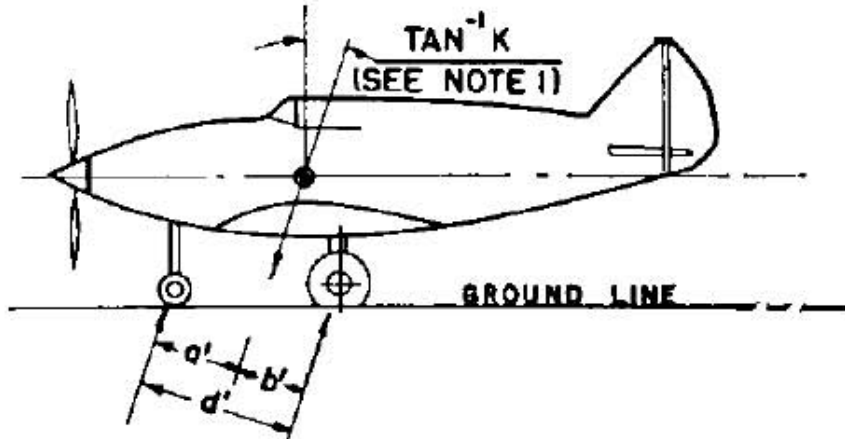
Note (2). For the purpose of design, the maximum load factor is assumed to occur throughout the shock absorber stroke from 25 percent deflection to 100 percent deflection unless otherwise shown and the load factor must be used with whatever shock absorber extension is most critical for each element of the landing gear.

Note (3). Unbalanced moments must be balanced by a rational or conservative method.

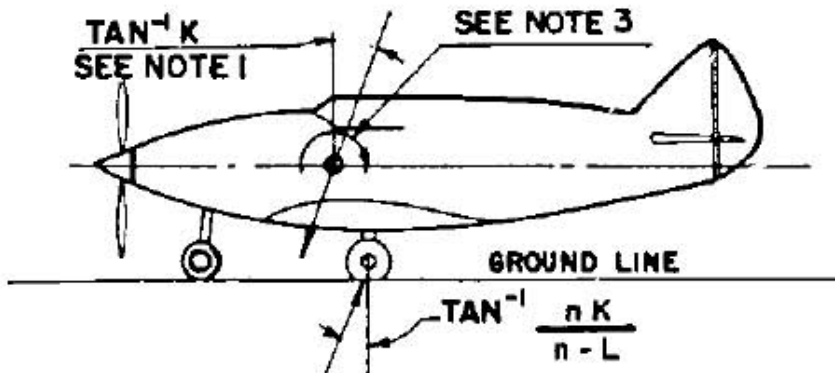
Note (4). L is defined in §23.735(b).

Note (5). n is the limit inertia load factor, at the c.g. of the airplane, selected under §23.473 (d), (f), and (g).

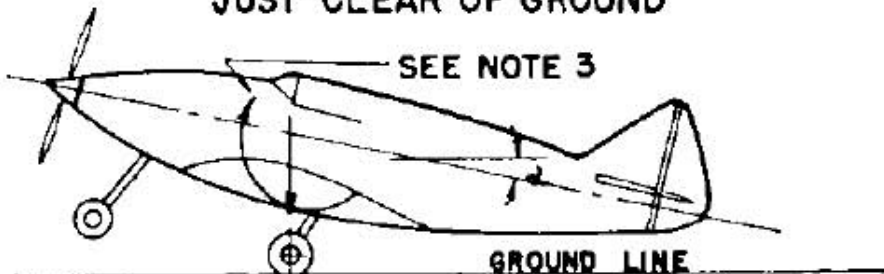
NOSE WHEEL TYPE



LEVEL LANDING WITH INCLINED REACTIONS



LEVEL LANDING WITH NOSE WHEEL JUST CLEAR OF GROUND



Note: See §23.481(a)(2)

TAIL DOWN LANDING